2004

Diffusional Interactions at Dual Disk Microelectrodes: Comparison of Experiment with Three-dimensional Random Walk Simulations

John E. Baur
Illinois State University, jebaur@ilstu.edu

Perry N. Motsegood
Illinois State University

DIFFUSIONAL INTERACTIONS AT DUAL DISK MICROELECTRODES: COMPARISON OF EXPERIMENT WITH THREE-DIMENSIONAL RANDOM WALK SIMULATIONS

John E. Baur[*] and Perry N. Motsegood[a]
Department of Chemistry
Illinois State University
Normal, IL 61790-4160, USA

Email: jebaur@ilstu.edu
Telephone: +1 (309)438-2663
Fax: +1 (309)438-5538

Abstract

Three dimensional random walk simulations were used to model the diffusional interactions between coplanar dual disk microelectrodes. Working curves for the dependence of shielding factor, collection efficiency, and amplification factor on the size of the gap between the electrodes were developed. The simulations showed that when the gap size was ≥ 22 radii, the electrodes could be considered as independent and diffusionally isolated. Empirical equations for determining the gap size from simple shielding and generator-collector experiments were established. The simulation was used to model the collector electrode response for square waves of various frequencies applied to the generator electrode. Simulation results were in excellent agreement with the experimental results for several dual disk electrodes having various gap sizes.

Keywords: chronoamperometry; simulation; microdisk electrode; diffusion; dual electrode; carbon fiber electrode; simulation; random walk

[*] Corresponding author. E-mail: jebaur@ilstu.edu
[a] Present address: MRM Corp., 101 W. Tomaras Ave., Savoy, IL 61874

1. Introduction

Probes having multiple independent microelectrodes in a single device are useful for detecting multiple species in solution [1], generating electrochemiluminescence [2-4], conducting diffusion layer titrations [5-7], and for parallel imaging in scanning electrochemical microscopy (SECM) [8]. In each of these applications, it is critical to understand the diffusional interaction between the individual electrodes so that crosstalk can be minimized (when making independent measurements) or maximized (for electrochemiluminescence and diffusion layer titrations). For some types of multi-electrode probes, such as the dual microband [5-7, 9, 10] and microring-disk [11, 12] electrodes, diffusional interactions have been modeled using computer simulations because their geometry can be reduced to two dimensions. However many other probes lack this symmetry and therefore modeling the diffusional interaction must be done in three dimensions.

A simple example of a geometry that must be solved in three dimensions is the dual disk microelectrode [13-16]. This device has two coplanar disk electrodes (10 μm diameter) separated by a gap that during fabrication is adjustable in size from <1 μm to > 50 μm. Because of this variable gap size, the degree of the diffusional interactions can be studied experimentally under different conditions. Additionally, this relatively simple geometry may be used as a model for more complex devices having multiple coplanar disk electrodes [8, 17, 18].

The boundary element method (BEM) [19-25] is becoming increasingly popular for modeling electrochemical systems, and has recently been applied to three-dimensional simulations of nonsymmetrical geometries [19, 21, 24, 25]. Qiu and Fisher recently used the BEM to model chronoamperometry at dual disk electrodes [21, 24] but they did not address shielding or correlate the simulation results with experimental data. While the BEM is powerful, it requires a high level of programming and mathematical sophistication. A simpler approach for modeling complex systems is the random walk, a method that has been applied to diffusionally interacting microelectrodes in two dimensions [26, 27] and to electrodeposition [28-33] and neurotransmitter dynamics [34-37] in three dimensions. Yet despite their simplicity, random walk simulations can yield accurate results for complex processes. Their chief disadvantage, computational inefficiency, is lessened in severity owing to the accessibility of ever more powerful computers.

In this work we adapt the three-dimensional random walk detailed by Nagy, et al. [38] to model diffusional interaction between coplanar dual disk microelectrodes. The effect of the gap size on shielding, collection efficiency, and amplification factor are investigated, and working curves are developed so that this gap size can be calculated from simple experimental measurements. Although this approach is semi-empirical, we demonstrate that the results are accurate by comparing them to the BEM results of Qiu and Fisher [24] and to experimental results for several electrodes having different gap sizes. Finally, the flexibility of the technique is demonstrated by simulating a generator-collector experiment in which a square wave is applied to one electrode of the pair.

2. Simulation

Fig. 1 shows the simulation volume, a rectangular box with dimensions defined by the sizes of the individual electrodes. The two electrodes having radii a_1 and a_2 (by definition $a_1 > a_2$ if the electrodes have unequal sizes) are separated by a gap distance of d and embedded in an infinite insulating plane. An integer, M, is used to set the minimum number of electrode radii between walls of the box and the electrode center. Thus the height of the box, z, is Ma_1 and the width, y, is $2Ma_1$. The box length, x, is dependent upon d and is given by $Ma_1 + (a_1 + d + a_2) + Ma_2 = (M + 1)(a_1 + a_2) + d$. Adjusting the value of M is a convenient way to change the simulation volume.

It is convenient to work with dimensionless variables so that a single set of simulation conditions can describe several related situations. To do this, the length variables a_1, a_2, d, x, y, and z are normalized by a unit length, Δl, that corresponds to the distance for a single step of the random walk. The reduced quantities are expressed as α_1, α_2, δ, X, Y, and Z, respectively. Using these variables the dimensions of the box can be expressed as:

$$X = \frac{x}{\Delta l} = \frac{(M+1)(a_1 + a_2) + d}{\Delta l} = (M+1)(\alpha_1 + \alpha_2) + \delta \tag{1}$$

$$Y = \frac{y}{\Delta l} = \frac{2Ma_1}{\Delta l} = 2M\alpha_1 \tag{2}$$

$$Z = \frac{z}{\Delta l} = \frac{Ma_1}{\Delta l} = M\alpha_1 \tag{3}$$

The number of volume elements (i.e. positions inside the box with unique values of X, Y, and Z), V, is therefore the product of these dimensionless lengths:

$$V = XYZ = \frac{xyz}{\Delta l^3} = 2M^3(\alpha_1^2\alpha_2 + \alpha_1^3) + 2M^2(\alpha_1^2\delta + \alpha_1^3 + \alpha_1^2\alpha_2) \quad (4)$$

This relation shows that the number of volume elements, and thus calculation time, is approximately proportional to M^3 but inversely proportional to Δl^3.

At the beginning of the simulation, a defined number of particles, N_0, are randomly positioned within individual volume elements throughout the simulation space. It is possible for multiple particles to occupy the same volume element. The occupancy ratio, ρ, is defined as the ratio of the total number of particles initially present to the number of volume elements in the simulation space, and is therefore analogous to concentration:

$$\rho = \frac{N_0}{XYZ} = \frac{N_0}{V} \quad (5)$$

During each step of the random walk, every particle is moved to the adjacent volume element in a randomly selected direction ($\pm X$, $\pm Y$, or $\pm Z$). The duration of a step is defined by a dimensionless value, T, which is related to the time for the step in seconds, t, and the unit length, Δl, by the diffusion coefficient [38]:

$$T = \frac{6Dt}{\Delta l^2} \quad (6)$$

This relation allows conversion between simulation time and seconds for an analyte with a known diffusion coefficient, D.

In contrast to the work of Nagy, et al. [38] particles are not removed from the simulation after undergoing a redox reaction. Instead, the "oxidation state" for each particle is tracked using an additional variable so that a particle reduced at one electrode can later be oxidized if it strikes an electrode poised at the appropriate potential (and vice versa). This approach is necessary for modeling diffusional interactions and has the advantages that multiple redox states and more complex potential waveforms can be readily incorporated. The drawback is that longer calculation times result because the number of particles remains constant and additional conditions must be tested for every particle during each iteration.

A reduction (or oxidation) event is recorded whenever a particle of the appropriate oxidation state enters a volume element directly above one of the electrodes and the potential of that electrode is sufficient to cause the reaction to occur. This potential dependence is modeled by way of a reaction probability at a given applied potential, $P(E)$, for a nernstian system:

$$P(E) = \frac{1}{\exp\left(\frac{\pm nF(E - E_{1/2})}{RT}\right) + 1} \quad (7)$$

where the exponential term is + for a reduction and - for an oxidation. Although this allows for simulating currents near $E_{1/2}$, for this work all experimental and simulated potentials were sufficiently far from $E_{1/2}$ so that faradaic currents were diffusion limited.

The sum of all reduction events during a given step of the random walk is taken as the current for that step. When a particle reaches one of the boundaries of the simulation box it is treated differently depending on which boundary is reached [38]. Particles that would pass through a side wall of the box are allowed to re-enter the opposite wall, and those that pass through the top of the box are replaced at a random *xy* position on the top volume element. Finally, particles are not allowed pass through the plane of the electrode.

All results shown are the average of 100 individual simulations. Unless otherwise noted, 25-point moving averages were applied to improve the signal to noise ratio. This moving average had no appreciable effect on the quantitative determination of the simulation current, as these measurements were made at long times where the currents were essentially time independent. Simulations were written in Microsoft Visual Basic 6.0. The time required for the simulations depended upon the specified values of d, ρ, and M, but was typically 15 – 30 min per individual simulation (Windows XP-based personal computers with AMD Athlon XP 2100+ CPU and 512 MB of RAM).

3. Experimental

Dual carbon fiber electrodes were prepared as described previously. Briefly, individual carbon fibers with nominal radii of 5 μm (Thornel P-55, Cytec, Greenville, SC, USA) were inserted into both sides of theta glass capillaries (World Precision Instruments, Sarasota, FL, USA), then the capillaries were tapered to a fine tip with a pipette puller (Narishige, Tokyo, Japan). The tip was then trimmed with a scalpel and the fibers were sealed in place with epoxy (Epon 828, Miller-Stephenson, Danbury, CT, USA). To ensure that the electrode tip was flat and that the two electrodes were coplanar, the electrode tip was polished vertically on a microelectrode beveller (Sutter Instrument Company, Novato, CA, USA). This polishing step afforded some control over the separation between the electrodes, as prolonged polishing increases the size of the tip and thus the spacing between the carbon fibers.

The SECM was similar to that described previously [39]. A 10 μm diameter Pt wire substrate was used for imaging the dual electrode tips. Generator-collector experiments were performed in the SECM cell using a separate locally-written program for collecting and analyzing the dual electrode data. It was necessary to move the dual electrode far (>1 mm) from the surface of the substrate to ensure the measurements took place in semi-infinite conditions.

All compounds were reagent grade used as received from commercial sources. Solutions of 1.0 mM $Ru(NH_3)_6^{3+}$ were made using pH 7.4 phosphate buffer prepared from 18 MΩ·cm deionized water (NanoPure System, Barnstead-Thermolyne, Dubuque, IA). The diffusion coefficient for $Ru(NH_3)_6^{3+}$ in this solution is 5.48×10^{-6} cm^2s^{-1} [40]. All potentials were recorded with respect to a silver/silver chloride reference electrode.

4. Results and Discussion

4.1. Validation of the Simulation

Since there is no established theoretical treatment for the diffusional interaction of coplanar dual disk microelectrodes, the algorithm and simulation space for the dual electrode geometry was first validated by setting only one of the two electrodes active. In this way, the simulated results could be compared to previous work [38] and the analytic expression developed by Shoup and Szabo for chronoamperometry at a disk microelectrode [41]. In terms of the dimensionless parameters described above, the Shoup and Szabo equation relates the dimensionless current, $I(T)$, to the dimensionless time, T [38]:

$$I(T) = \frac{4}{6}\rho\alpha\left[\frac{\pi}{4} + \frac{\sqrt{6\pi}\alpha}{4\sqrt{T}} + \left(1 - \frac{\pi}{4}\right)\exp\left(-\frac{\left(\sqrt{\pi} - 8\pi^{-3/2}\right)\sqrt{6}\alpha}{(4-\pi)\sqrt{T}}\right)\right] \tag{8}$$

and is accurate to within 0.6% for all values of T. Note that in this equation, T is dependent on the value of l chosen for a particular simulation (see Eq. 6). Fig. 2 compares simulated currents to that calculated using Eq. 8. This figure shows simulations both for a single disk electrode (gray line) and for a dual electrode having only one of the two electrodes active (black line) but in the simulation space of Fig. 1. The inset of Fig. 2 shows the same comparison at smaller values of T and without application of the 25-point moving average. Clearly, both simulations show excellent agreement with theory, and the simulations are indistinguishable from one another. Further, the application of the 25-point smooth merely improves the signal-to-noise ratio

without affecting simulation accuracy. These results indicate that the simulation routine can be applied to the dual electrode case with confidence.

For the simulation to approach physical reality, the size of the simulation space should be very large with respect to the electrode radius (i.e. $M \to \infty$) and the volume element size should approach the molecular scale (i.e. $\Delta l \to 0$). Clearly this is impractical since the number of particles would not be manageable (for a given value of ρ, N_0 is proportional to M^3 and inversely proportional to Δl^3) and the time modeled by a single step of the random walk (t in Eq. 6) would approach zero. Therefore values of the simulation variables must be selected to balance computation time and simulation accuracy. For this work, a unit length of 1 μm ($\Delta l = 10^{-4}$ cm) was selected and the values of the other variables were optimized.

Fig. 3A shows how the simulation accuracy and computation time depend on the simulation space size (in terms of M) for a single electrode active in the dual electrode simulation space. For this data the relative error was determined from the average residual of the entire simulation (T = 10,000) compared to the theoretical current calculated from Eq. 8. The error drops rapidly as the simulation space increases, reaching 1% when M = 10 and 0.3% at M = 14. The improvement in accuracy from M = 10 to M = 14 comes at the expense of a two-fold increase in computation time, therefore a compromise value of M = 12 (with an error of 0.6%, a value equivalent to the error of Eq. 8) [41] was chosen for all subsequent simulations.

Fig. 3B shows the effect of the occupancy ratio, ρ, on the simulation error and signal-to-noise ratio when M = 12. Although at lower values of occupancy ratio fewer particles encounter the electrode (and therefore the magnitude of the current decreases), the relative error is unaffected; it is below 0.7 % over the range of ρ = 0.05 to 0.5. However because fewer particles reach the electrode when ρ is small there are greater relative fluctuations in the simulated current, resulting in lower signal-to-noise ratios. While the signal-to-noise ratio depends upon $\sqrt{\rho}$, the increase in simulation time (which increases with ρ) with no improvement in accuracy means that there is little advantage of using a larger ρ. Therefore an occupancy ratio of 0.05 was used for all subsequent simulations.

4.2. Simulations of the diffusional interactions

The dependence of the diffusional interaction on the gap size between two microelectrodes having equal radii is explored in Figs. 4-6. These figures show representative simulations and working curves for shielding (Fig. 4), collection efficiency (Fig. 5), and amplification factor, or feedback (Fig. 6) as a function of gap size. For the working curves, the distance between electrode edges, δ, was normalized by α_1. Note that this normalized gap size, designated as g, is the same whether dimensionless or spatial quantities are used. Panel A of each figure shows a simulation with $g = 0$, when the edges of the electrode are just touching but still operating independently. This represents the limiting case for the minimum possible electrode spacing and therefore the maximal overlap of the electrodes' diffusion layers. A simulation with $g = 22$ is shown in Panel B of each figure. At this value of g, the electrode centers are separated by $2M\alpha_1$ (where $M = 12$). This is analogous to two single-electrode simulation spaces with $M = 12$ sharing a common border, and thus diffusional interaction effects should be absent (within 1%). Panel C of each figure shows the working curves and the individual data points (open circles) from which the working curves were derived. Data from the BEM simulations of Qiu and Fisher [24] is included for comparison (filled squares).

Each data point of the working curves represents the average of 5 sets of 100 simulations. Error bars corresponding to the standard deviation of the 5 sets are included but in most cases are not visible because the range is smaller than the size of the data points. Values for the working curves were obtained by averaging currents over the range of T from 8,250 to 9,900. It is instructive to express T in terms of τ, a commonly used dimensionless variable for disk microelectrodes [42]:

$$\tau = \frac{4Dt}{a^2} = \frac{2T}{3\alpha^2} \tag{9}$$

Therefore the data points were obtained over the range of τ from 220 to 264, which falls into the long time regime. At these values of τ, the current has decayed to within 5% of the steady-state value for a single disk microelectrode [41-43].

Shielding occurs when the same redox reaction occurs at two (or more) electrodes with overlapping diffusion layers and thus there is not sufficient solution species to sustain the theoretical steady-state current at both electrodes. Instead, the observed current is less than what it would be if there was no overlap of the diffusion layers. Shielding was simulated by simultaneously stepping the potential of both electrodes to the same value and summing all of

the reduction events occurring at the two electrodes. Comparison of this current to the sum of the current at two diffusionally isolated electrodes (gray lines in Fig. 4) allows the shielding effect to be visualized. Fig. 4A shows that when $g = 0$ an appreciable shielding effect is observed, which can be quantified by calculating a shielding factor, S:

$$S = \frac{I_{1+2}}{I_1 + I_2} \tag{10}$$

where I_{1+2} is the current observed at the electrode pair and I_1 and I_2 are the currents observed for electrodes 1 and 2, respectively, when they are diffusionally isolated from one another (i.e. $g \geq 22$). The maximum value of the shielding factor is 1 (completely isolated electrodes), and the minimum value, occurring at $g = 0$, was found to be 0.765. Figure 4B shows that when $g = 22$ the shielded current is indistinguishable from the unshielded current. The shielding factor calculated for this simulation is 1.00, indicating that there is no measurable diffusional interaction between the two electrodes. This is consistent with the previous determination that a simulation space having $M \geq 12$ yields accurate results.

Fig. 4C shows the working curve for the shielding factor over the range of g from 0 to 22. The shielding factor increases rapidly from 0.765 at $g = 0$ to 0.973 at $g = 8$. The working curve fits the empirical equation:

$$S = 0.766 + 0.233(1 - e^{-0.317g}) \tag{11}$$

with an R^2 value of 0.9955. The standard errors of the coefficients range from 0.7% to 8.4%. Rearranging this equation gives an expression that can be used to estimate g for an experimentally measured shielding factor:

$$g = -\left[4.60 + 3.16\ln(0.999 - S)\right] \approx -\left[4.6 + 3.2\ln(1 - S)\right] \tag{12}$$

This equation cannot be used when the shielding factor approaches 1, as the calculated gap size approaches ∞. Because of the asymptotic nature of the working curve, Eqs. 11 and 12 will be most useful for smaller values of g ($\lesssim 10$) where there is an appreciable change in S for a given change in g.

For the generator-collector experiment, the potential of one electrode is set to detect the reaction products of the other electrode, thus the original species is regenerated. This configuration was simulated by stepping the potential of one electrode to a value where species is reduced (or oxidized) while maintaining the potential of the other electrode at the initial

potential. The number of redox events at each electrode was tracked separately, giving separate simulated currents for the generator and collector electrodes. The ratio of the collector current, I_c, to the generator current, I_g, termed the collection efficiency, N, represents the fraction of generated species reaching the collector electrode. Fig. 5A shows the simulated generator and collector currents at $g = 0$, where the collection efficiency is maximum. Analysis of this data shows that this maximum value of the collection efficiency is 0.349, meaning that no more than 34.9% of the species produced at the generator electrode can be detected by the collector. Figure 5B shows that when g reaches 22 essentially no redox events are detected by the collector, as evidenced by the absence of collector current. In fact, over the entire duration of each simulation a total of only 2 particles (on average) of the appropriate oxidation state ever reached the collector. This is further support of the assertion that electrodes having $g = 22$ are diffusionally isolated.

The working curve for the generator-collector data is shown in Fig. 5C. This figure shows that the results from the random walk simulations are in good agreement with the BEM simulations of reference 24. The best fit to the random walk simulation data ($R^2 = 0.9997$) was a double exponential decay given by:

$$N = 0.164e^{-1.33g} + 0.185e^{-0.223g} \tag{13}$$

The standard errors on the coefficients range from 8.8% to 11.7%. Because it is not possible to solve Eq. 13 for g in terms of N, a new fit was made after making g the dependent variable and N the independent variable. The resulting empirical equation (having $R^2 = 0.9997$) can be used to calculate g from the measured collection efficiency:

$$g = 21.2e^{-179N} + 12.0e^{-13.9N} \tag{14}$$

where the standard errors on the coefficients range from 4.1% to 9.2%. For collection efficiencies > 0.03, the first term is negligible and the relation becomes:

$$g = 12.0e^{-13.9N} \tag{15}$$

As before, Eqs. 14 and 15 are most useful for determining gap sizes for electrodes with $g \lesssim 10$.

In the generator-collector experiment, species detected by the collector is reconverted to starting material and then a fraction of this regenerated starting material can diffuse back to the generator electrode. In essence, the steady-state generator current is enhanced because of the resulting increase in concentration. Fig. 6A demonstrates this effect; the generator current for an

electrode pair having $g = 0$ is significantly enhanced over the current expected for a single electrode. This effect can be quantified by the amplification factor, the ratio of the observed generator current, I_g, to the current for a single electrode of the same size, I_1. The maximum amplification factor, occurring when $g = 0$, was found to be 1.18. The simulations also show the expected dramatic dependence of the amplification factor on g; the working curve in Fig. 6C shows that the amplification factor drops to less than 1.02 at $g = 0.4$. The simulated values of amplification factor show less precision than the simulated values of shielding factor and collection efficiency, but there is still good agreement between the random walk results and those of reference 24. Because the amplification factor only changes significantly at very small gap sizes, it is of little practical use for determining g and therefore the data was not fit to a working curve. Despite the relative imprecision of the simulation of the amplification factor, Fig. 6D shows that the simulations correctly predict the expected relationship between the inverse amplification factor and the collection efficiency [44].

4.3. Comparison between simulations and experimental data

The results of diffusional interaction experiments for 10 different dual carbon fiber disk electrodes are summarized in Fig. 7 and Table 1. These results are the averages of 5 replicate experiments for each electrode. The gap size of each electrode was measured (in μm) using the SECM as described previously [13] and then normalized by the nominal electrode radius to find g. For this determination currents were averaged over the same range of T as the working curves (8,250 to 9,900). In Fig. 7 the experimental data is overlaid either on the working curves obtained from simulations (Figs. 7A and B) or the individual simulation data points (Figs. 7C and D). The data for shielding (Fig. 7A) and collection efficiency (Fig. 7B), show close agreement with the working curve over the range of gap sizes used. It is apparent from Fig. 7C that the experimental amplification factors show significant scatter, but there is general agreement between the data and the simulations. For the electrode with the smallest gap size ($g = 0.46$) the experimentally-determined amplification factor is only 1.05, and it drops to < 1.01 for electrodes having g near 2. The combination of this steep dependence on g with the scatter between the simulations and experimental data reinforces the conclusion that the amplification factor is unsuitable for determining g.

Table 1. Comparison of measured and calculated values of g for 10 dual carbon fiber electrodes.

	Measured			Calculated g			Difference[c]
Electrode	g	S	N	From S[a]	From N[b]	Average	
1	0.46	0.82	0.22	0.75	0.58	0.66	-0.21
2	1.18	0.838	0.202	1.17	0.72	0.95	0.24
3	1.47	0.871	0.184	1.90	0.93	1.41	0.05
4	1.96	0.887	0.128	2.32	2.02	2.17	-0.21
5	2.13	0.895	0.119	2.55	2.29	2.42	-0.29
6	3.36	0.894	0.088	2.52	3.51	3.02	0.34
7	3.93	0.935	0.077	4.09	4.13	4.11	-0.18
8	5.42	0.963	0.050	5.91	5.99	5.95	-0.53
9	7.44	0.968	0.034	6.39	7.59	6.99	0.45
10	8.22	0.994	0.026	12.2	8.61	10.4	-2.2

[a]Calculated from the measured shielding factor, S, using Eq. 12.
[b]Calculated from the measured collection efficiency, N, using Eq. 14.
[c](Measured g) – (average calculated g)

In Table 1 values of the gap size calculated from Eqs. 12 and 14 are compared with the gap size measured with SECM. Except for the electrode with the largest value of g (Electrode 10), the difference between the average calculated g and the measured g is less than 0.53. In fact, the difference is approx. 0.25 or less for the electrodes with a measured g of less than 2. The average relative difference between the values of g for all 10 electrodes was 6%, which is reasonable given the accuracy of the coefficients in the empirical equations. A close examination of the data in Table 1 also reveals that for electrodes with the largest gap size (Electrodes 9 and 10) the value of g calculated from the collection efficiency (Eq. 14 or 15) is still reasonably accurate (≤ 5% difference). Based upon these results, we recommend that the electrode spacing be determined from measurements of collection efficiency for electrodes with wider gaps ($g \gtrsim 5$) and from either collection efficiency or shielding factor (Eq. 12) for electrodes with narrower gaps ($g \lesssim 5$).

4.4. Multiple potential steps

To demonstrate the flexibility of these simulations, the generator-collector experiment was modeled for square waves of different frequencies applied to the generator electrode. The potential limits of the square wave were well above and below the $E_{½}$ of the redox couple so that all currents were diffusion-limited. Figs. 8 and 9 show the experimental and simulated collector currents, respectively, for an electrode with a narrow gap (g = 1.1, black line) and an electrode with a wide gap (g = 7.2, gray line) when square waves between 0.2 and 5.0 Hz are applied to the generator.

These figures demonstrate the excellent agreement between the experimental data and the simulations at all four frequencies. For the electrode with the smaller gap, the time required to diffuse to the collector is small, and so a rapid rise to a steady-state collector response is observed (Figs. 8A and 9A). At higher frequencies, the collector current does not reach steady state and therefore resembles a filtered square wave, the magnitude of which decreases with increasing square wave frequency [13]. The simulations accurately model these changes in shape and amplitude. For the electrode with the wider gap, the time required to diffuse across the gap is significantly longer and so even at 0.2 Hz a steady state collector current is not reached (Figs. 8A and 9A). In fact a delay between the application of the potential to the generator and the collector response is evident, consistent with the time required for product to diffuse across the gap. At higher frequencies the oscillations in the collector current are greatly damped; at 1.0 Hz the oscillations are still evident but at 2 Hz are almost completely absent and instead the collector current slowly increases from zero. At 5 Hz only a slight rise in the collector current is detectable. The simulations shown in Fig. 9 also accurately model these behaviors for the wider gap. At 0.2 Hz, the delay in collector response is present, oscillations are visible at 1 Hz, and only modest, oscillation-free increases are evident at 2 and 5 Hz. These results further demonstrate the usefulness of this simulation method for modeling the response of the dual electrodes.

5. Conclusions

Random walk simulations, despite their simplicity and computational inefficiency, can be used for making theoretical approximations of the diffusional interaction between closely spaced disk electrodes. Using this technique, empirical working curves were developed for the dependence of collection efficiency and shielding factor on gap size when the two electrodes

have equal radii. These working curves are useful for calculating the gap size between two adjacent disk electrodes from simple shielding and/or generator-collector experiments. Alternatively, the degree of diffusional interaction can be determined if the gap size is known. Only when $g \geq 22$ do the electrodes behave as if they are completely isolated. These results will be useful for predicting the diffusional interactions of more complex devices having coplanar disk microelectrodes.

6. References

1. B. L. Whited, P. N. Motsegood, and J. E. Baur, J. Chromatogr. A 771 (1997) 89.
2. C. Amatore, B. Fosset, K. M. Maness, and R. M. Wightman, Anal. Chem. 65 (1993) 2311.
3. C. Amatore, A. Oleinick, and I. Svir, Electrochem. Comm. 5 (2003) 989.
4. J. E. Bartelt, S. M. Drew, and R. M. Wightman, J. Electrochem. Soc. 139 (1992) 70.
5. H. Rajantie and D. E. Williams, Analyst 126 (2001) 1882.
6. I. B. Svir, A. I. Oleinick, and R. G. Compton, J. Electroanal. Chem. 560 (2003) 117.
7. H. Rajantie, J. Strutwolf, and D. E. Williams, J. Electroanal. Chem. 500 (2001) 108.
8. A. Barker, P. R. Unwin, J. W. Gardner, and H. Rieley, Electrochem. Comm. 6 (2004) 91.
9. J. E. Bartelt, M. R. Deakin, C. Amatore, and R. M. Wightman, Anal. Chem. 60 (1988) 2167.
10. P. M. Kovach, W. L. Caudill, D. G. Peters, and R. M. Wightman, J. Electroanal. Chem. 185 (1985) 285.
11. P. Liljeroth, C. Johans, C. J. Slevin, B. M. Quinn, and K. Kontturi, Anal. Chem. 74 (2002) 1972.
12. P. Liljeroth, C. Johans, C. J. Slevin, B. M. Quinn, and K. Kontturi, Electrochem. Comm. 4 (2002) 67.
13. J. E. Baur, H. M. Miller, and M. A. Ritchason, Anal. Chim. Acta 397 (1999) 123.
14. F.-M. Matysik, Electrochim. Acta 42 (1997) 3113.
15. T. Yasukawa, T. Kaya, and T. Matsue, Anal. Chem. 71 (1999) 4637.
16. C. Zhang and X. Zhou, J. Electroanal. Chem. 415 (1996) 65.
17. E. Nebling, T. Grunwald, J. Alabers, P. Schafer, and R. Hintsche, Anal. Chem. 76 (2004) 689.
18. C. G. Zoski, N. Simjee, O. Guenat, and M. Koudelka-Hep, Anal. Chem. 76 (2004) 62.
19. O. Sklyar, J. Ufheil, J. Heinze, and G. Wittstock, Electrochim. Acta 49 (2003) 117.
20. Q. Fulian and A. C. Fisher, J. Phys. Chem. B 102 (1998) 9647.

21. Q. Fulian, N. A. Williams, and A. C. Fisher, Electrochem. Comm. 1 (1999) 124.
22. Q. Fulian, A. C. Fisher, and G. Denuault, J. Phys. Chem. B 103 (1999) 4393.
23. Q. Fulian, A. C. Fisher, and G. Denuault, J. Phys. Chem. B 103 (1999) 4387.
24. F. L. Qiu and A. C. Fisher, Electrochem. Comm. 5 (2003) 87.
25. O. Sklyar and G. Wittstock, J. Phys. Chem. B 106 (2002) 7499.
26. S. Licht, V. Cammarata, and M. S. Wrighton, Science 243 (1989) 1176.
27. S. Licht, V. Cammarata, and M. S. Wrighton, J. Phys. Chem. 94 (1990) 6133.
28. M. C. Gimenez, M. G. D. Popolo, and E. P. M. Leiva, Langmuir 2002 (2002) 9087.
29. M. C. Gimenez, M. G. D. Popolo, and E. P. M. Leiva, Electrochim. Acta 45 (1999) 699.
30. D. Y. Li and J. A. Szpunar, J. Electron. Mat. 22 (1993) 653.
31. T. J. Pricer, M. J. Kushner, and R. C. Alkire, J. Electrochem. Soc. 149 (2002) C406.
32. V. Tsakova and A. Milchev, J. Electroanal. Chem. 451 (1998) 211.
33. D. Y. Li and J. A. Szpunar, Electrochim. Acta 42 (1996) 37.
34. P. J. Kruk, H. Korn, and D. S. Faber, Biophys. J. 73 (1997) 2874.
35. C. Nicholson, K. C. Chen, S. Hrabetova, and L. Tao, Prog. Brain Res. 125 (2000) 129.
36. H. Yang, J. L. Peters, C. Allen, S.-S. Chern, R. D. Coalson, and A. C. Michael, Anal. Chem. 72 (2000) 2042.
37. H. C. Berg, Random Walks in Biology, Princeton University Press, Princeton, NJ, 1993.
38. G. Nagy, Y. Sugimoto, and G. Denuault, J. Electroanal. Chem. 433 (1997) 167.
39. D. O. Wipf, F. Ge, T. W. Spaine, and J. E. Baur, Anal. Chem. 72 (2000) 4921.
40. J. E. Baur and R. M. Wightman, J. Electroanal. Chem. 305 (1991) 73.
41. D. Shoup and A. Szabo, J. Electroanal. Chem. 140 (1982) 237.
42. A. J. Bard and L. R. Faulkner, Electrochemical Methods: Fundamentals and Applications, Second Edition, John Wiley & Sons, Inc., New York, 2001.
43. K. Aoki and J. Osteryoung, J. Electroanal. Chem 122 (1981) 19.
44. B. Fosset, C. A. Amatore, J. E. Bartelt, A. C. Michael, and R. M. Wightman, Anal. Chem. 63 (1991) 306.

Appendix. List of Symbols

Symbol	Description	Units
a_1	Radius of the larger electrode	cm
a_2	Radius of the smaller electrode	cm
D	Diffusion coefficient	$cm^2\ s^{-1}$
d	Distance between the electrode edges	cm
E	Electrode potential	V
$E_{1/2}$	Half-wave potential	V
F	Faraday constant	$C\ mol^{-1}$
g	Distance between electrode edges (d) normalized by the larger electrode radius (a_1)	dimensionless
I_1	Simulation current for the larger electrode when diffusionally isolated	dimensionless
I_2	Simulation current for the smaller electrode when diffusionally isolated	dimensionless
I_g	Simulation current for the generator electrode	dimensionless
I_c	Simulation current for the collector electrode	dimensionless
Δl	Unit distance (distance moved per step of the random walk)	cm
M	Integer that defines the minimum distance (in radii, a_1) between an electrode center and the edge of the simulation space	dimensionless
N	Collection efficiency	dimensionless
N_0	Number of particles initially present in the simulation	dimensionless
n	Stoichiometric number of electrons involved in an electrode reaction	dimensionless
P	Probability of a reduction (or oxidation) event	dimensionless
R	Molar gas constant	$J\ mol^{-1}\ K^{-1}$
S	Shielding factor	dimensionless
t	Time per simulation step	s
T	Time per simulation iteration	dimensionless
T	Temperature	K
V	Number of volume elements	dimensionless
x, y, z	Dimensions of the simulation space	cm
X, Y, Z	Dimensions of the simulation space	dimensionless
α_1	Electrode radius of the larger electrode	dimensionless
α_2	Electrode radius of the smaller electrode	dimensionless
δ	Distance between edges of the two electrodes	dimensionless
ρ	Occupancy ratio	dimensionless
τ	Square of the diffusion length to disk radius ratio	dimensionless

Figures

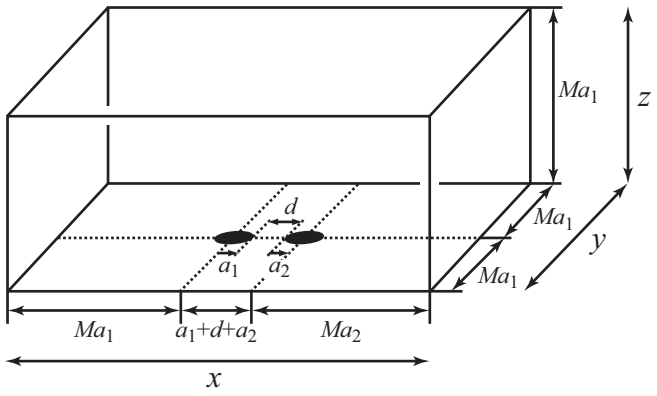

Figure 1. Simulation space for the dual disk microelectrodes.

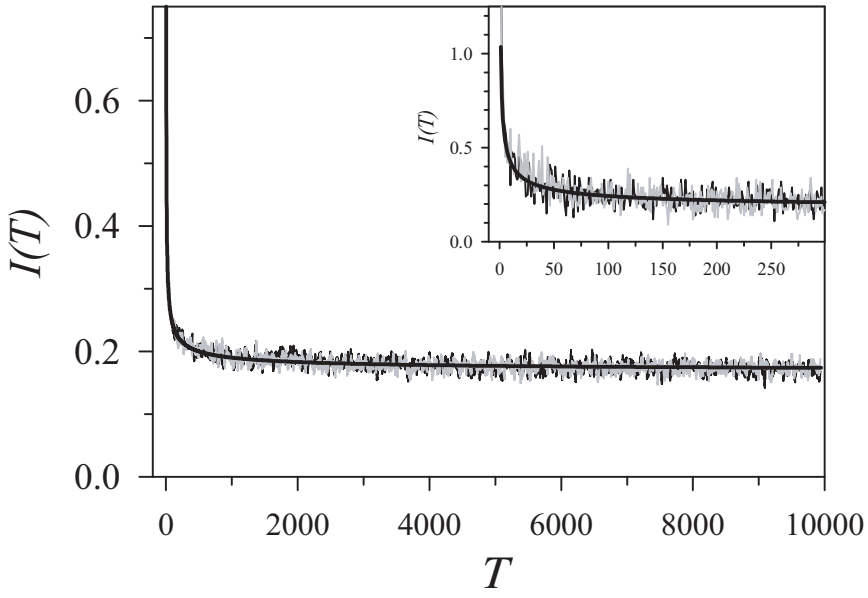

Figure 2. Comparison of simulated and theoretical chronoamperometry currents. The smooth black line is the theoretical current for a disk electrode calculated from Eq. 8, the noisy gray line is the random walk simulation for a single disk electrode, and the noisy black line is the simulation for one active disk electrode in the dual electrode geometry. Inset: expanded detail of the three curves at small values of T but without applying the 25-point moving average. Conditions: Average of 100 simulations with $\rho = 0.05$, $M = 12$, and $\alpha = 5$. For the single disk geometry $X = Y = 120$ and $Z = 60$; for the dual disk geometry $\alpha_1 = 5$, $\delta = 2$, $X = 132$, $Y = 120$, and $Z = 60$.

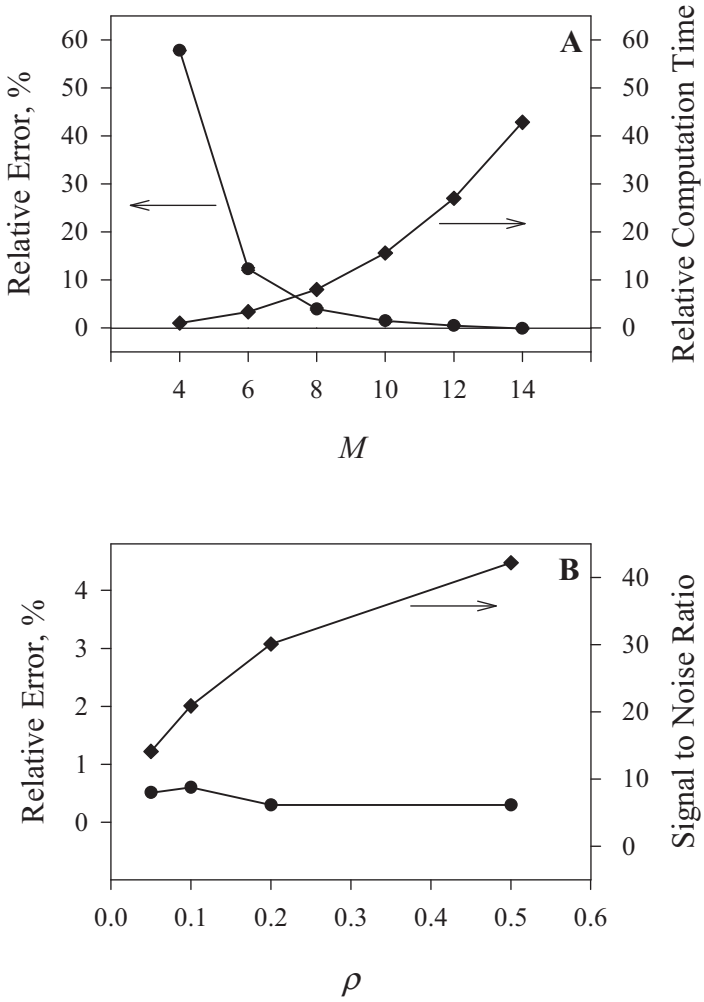

Figure 3. Effect of selected simulation parameters for a single active electrode in the dual electrode geometry. (A) Effect of simulation volume (in terms of the radius multiplier, M) on the relative error and calculation time. (B) The effect of the occupancy ratio, ρ, on the error and signal-to-noise ratio of the simulation. Conditions: Average of 100 simulations. For (A) $\rho = 0.05$, $\delta = 2$, $\alpha = 5$, and X, Y, and Z vary with M as described in Eq. 1 – 3. For (B) $M = 12$, $\delta = 2$, $\alpha = 5$, $X = 132$, $Y = 120$, and $Z = 60$.

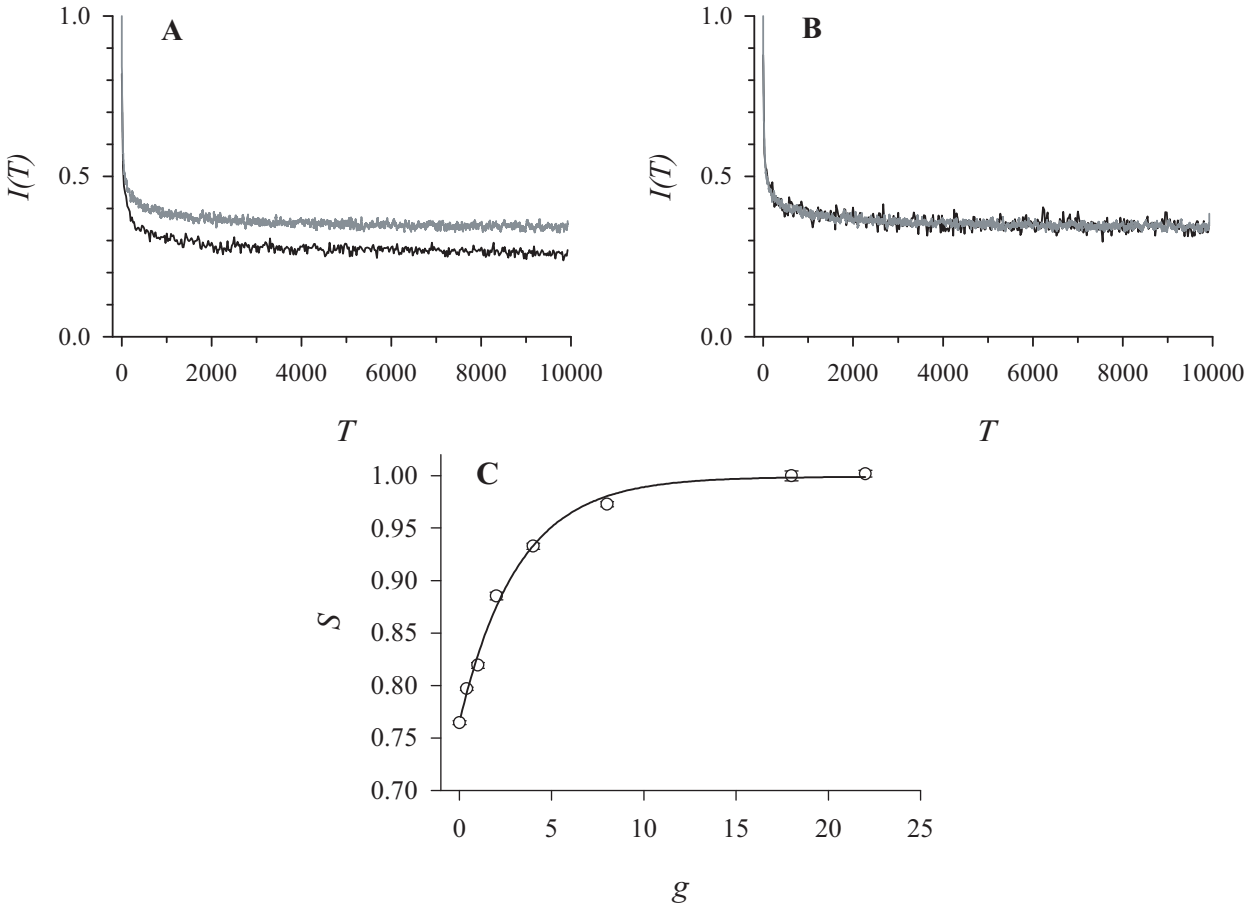

Figure 4. Simulations of the effect of electrode spacing on shielding. (A) Simulated chronoamperograms for a dual disk electrode with $g = 0$ (black line) and two electrodes diffusionally isolated from each other (gray line). (B) Same as in A except the black line corresponds to $g = 22$. (C) Simulated working curve for the dependence of the shielding factor on g. The line is a plot of Eq. 11. Conditions: Average of 100 simulations and $\rho = 0.05$. For the single disk simulations, $\alpha = 5$, $X = Y = 120$, and $Z = 60$. For the dual disk simulations, $\alpha_1 = \alpha_2 = 5$, $X = 130 + \alpha_1 g$, $Y = 120$, and $Z = 60$.

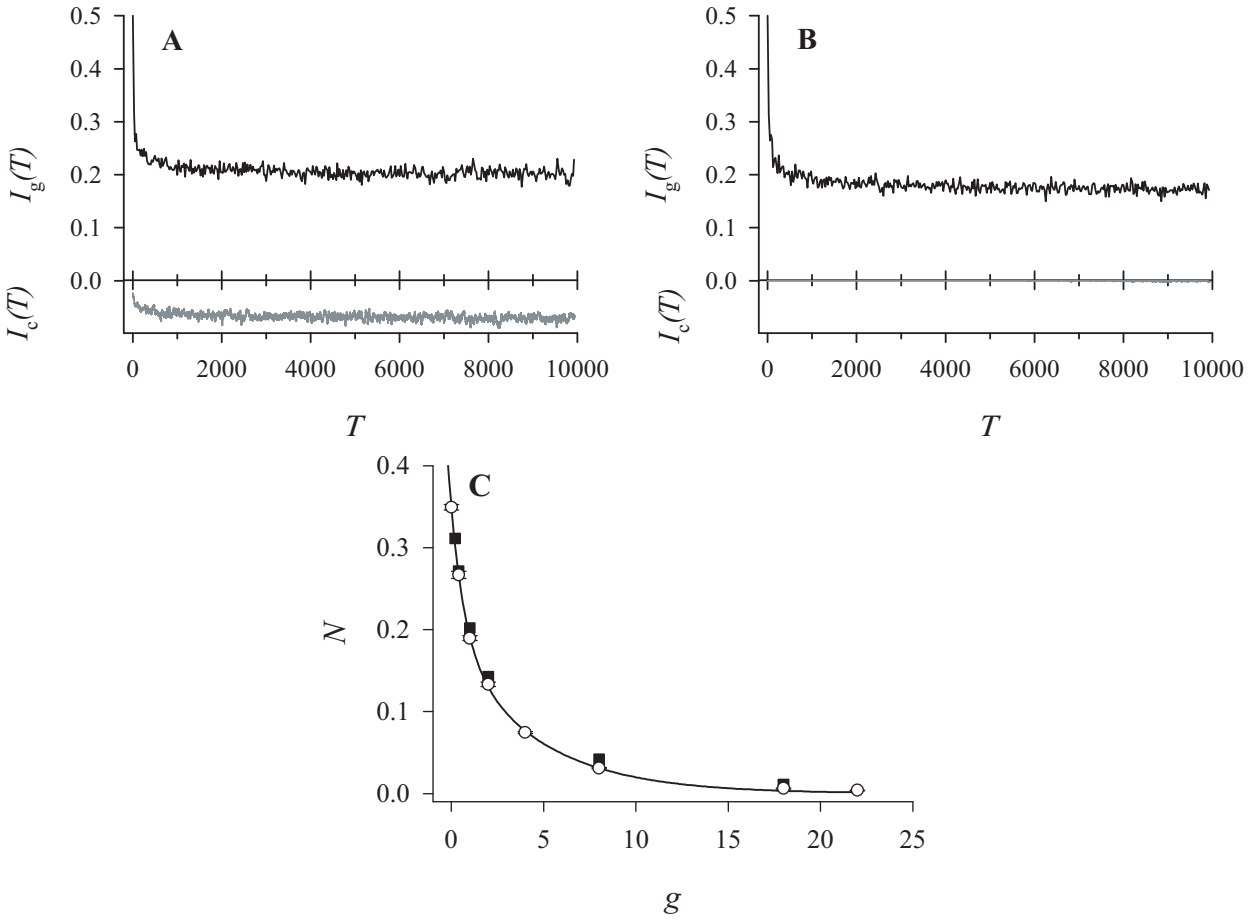

Figure 5. Generator-collector simulations of the effect of electrode spacing on collector current. (A) Simulated current for the generator current (black line) and the collector current (gray line) for $g = 0$ for a potential step at applied to the generator electrode. (B) Same as in A except $g = 22$. (C) Simulated working curve for the dependence of the collection efficiency on g. Open circles are from random walk simulations, filled squares are from reference 24, and the line is a plot of Eq. 13. Conditions: Average of 100 simulations, $\alpha_1 = \alpha_2 = 5$, $\rho = 0.05$, $X = 130 + \alpha_1 g$, $Y = 120$, and $Z = 60$.

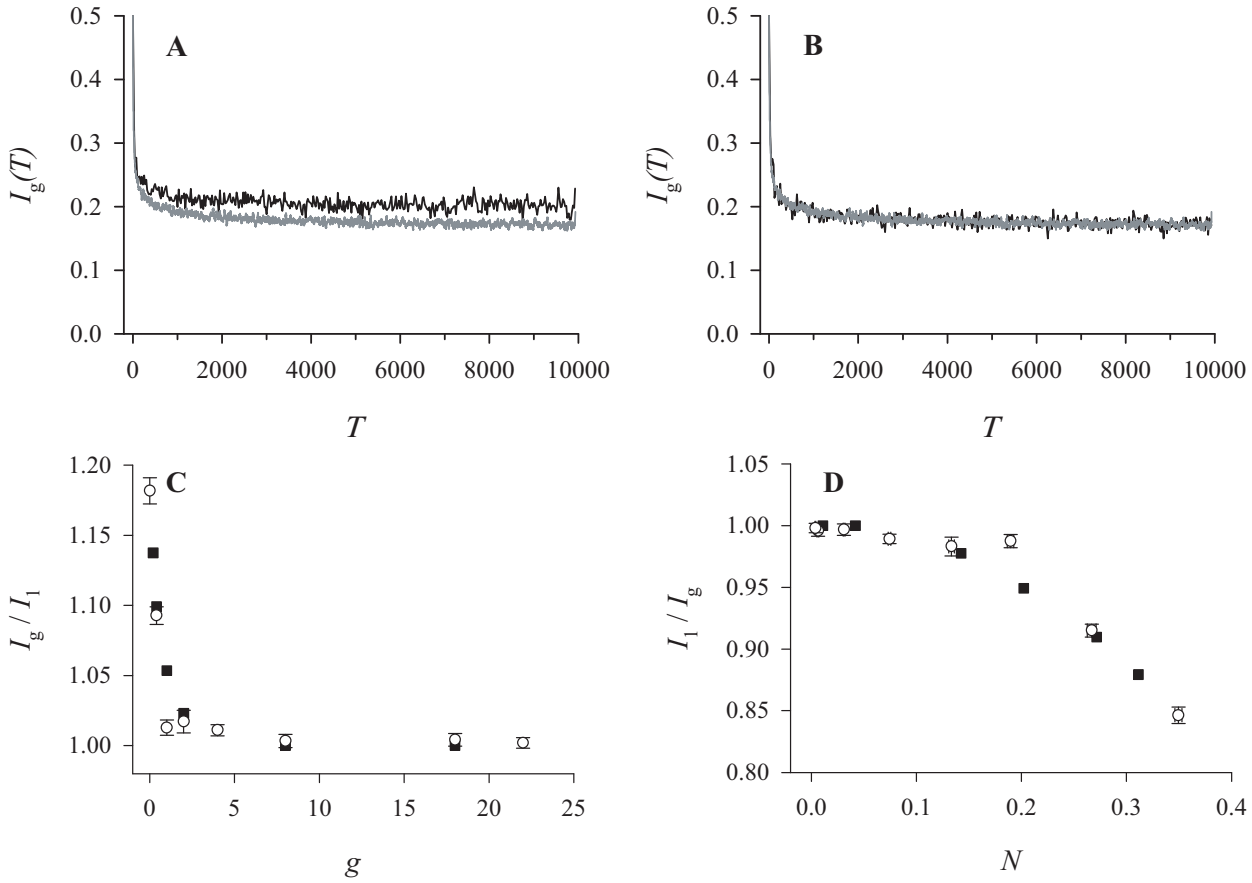

Figure 6. Simulations of the effect of electrode spacing on the amplification factor. (A) Simulated chronoamperograms for the generator current with $g = 0$ (black line) and for a single isolated electrode (gray line). (B) Same as in A except the black line corresponds to $g = 22$. (C) Simulated working curve for the dependence of the amplification factor on g. (D) Simulated working curve for the dependence of the inverse amplification factor on the collection efficiency. In C and D, open circles are from random walk simulations, filled squares are from reference 24, and error bars represent the standard deviation for five replicate sets of simulations. Conditions: Average of 100 simulations and $\rho = 0.05$. For the single disk simulations, $\alpha = 5$, $X = Y = 120$, and $Z = 60$. For the dual disk simulations, $\alpha_1 = \alpha_2 = 5$, $X = 130 + \alpha_1 g$, $Y = 120$, and $Z = 60$.

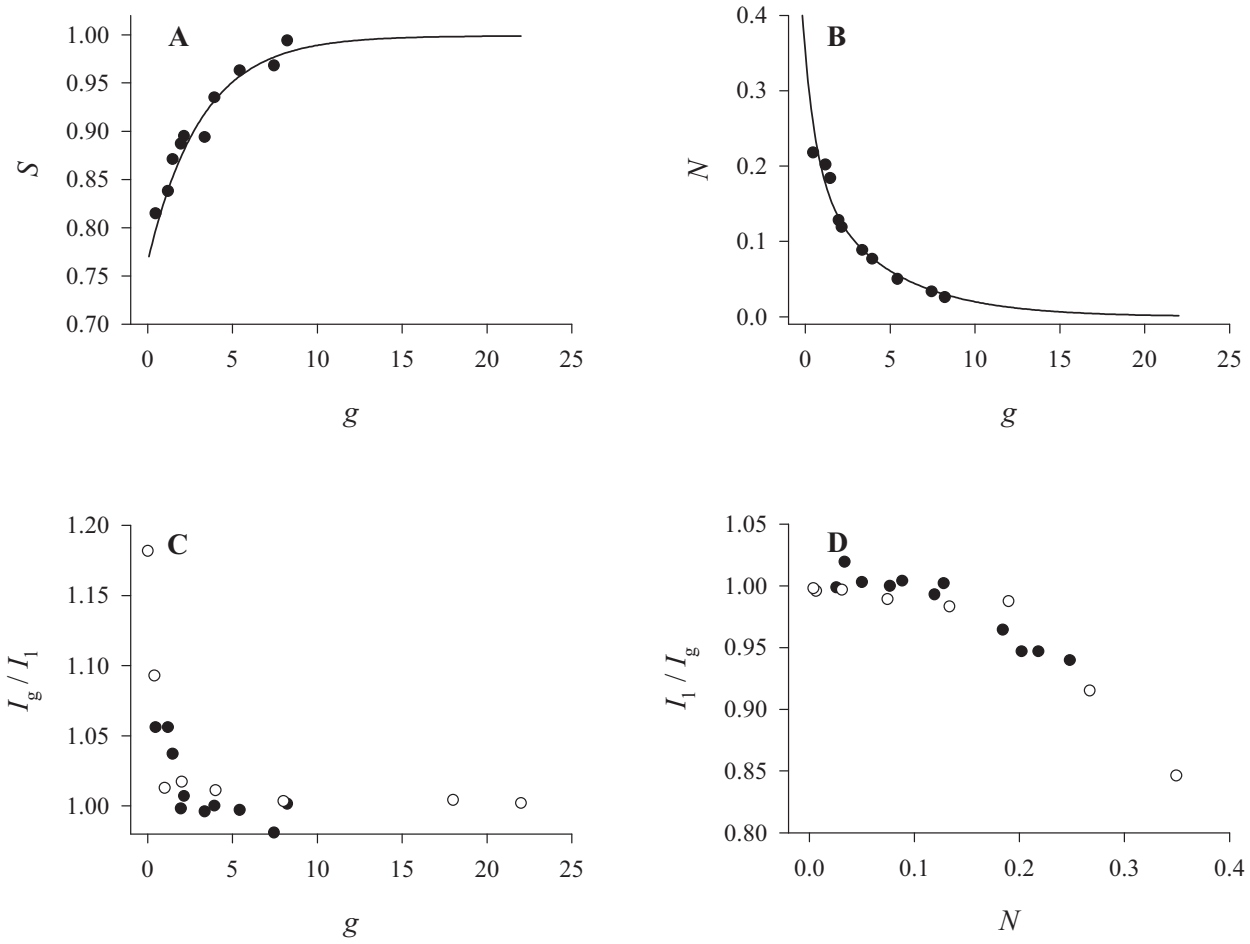

Figure 7. Comparison of the working curves from Figures 4-6 to the experimental results for 10 dual carbon fiber disk electrodes. Filled circles represent experimental data; solid lines and open circles represent simulation results. (A) Shielding factor, (B) collection efficiency, and (C) amplification factor. (D) Dependence of the inverse amplification factor on collection efficiency. Experimental conditions: 1.00 mM $Ru(NH_3)_6^{3+}$ in pH 7.4 phosphate buffer. The interelectrode spacing was measured by SECM.

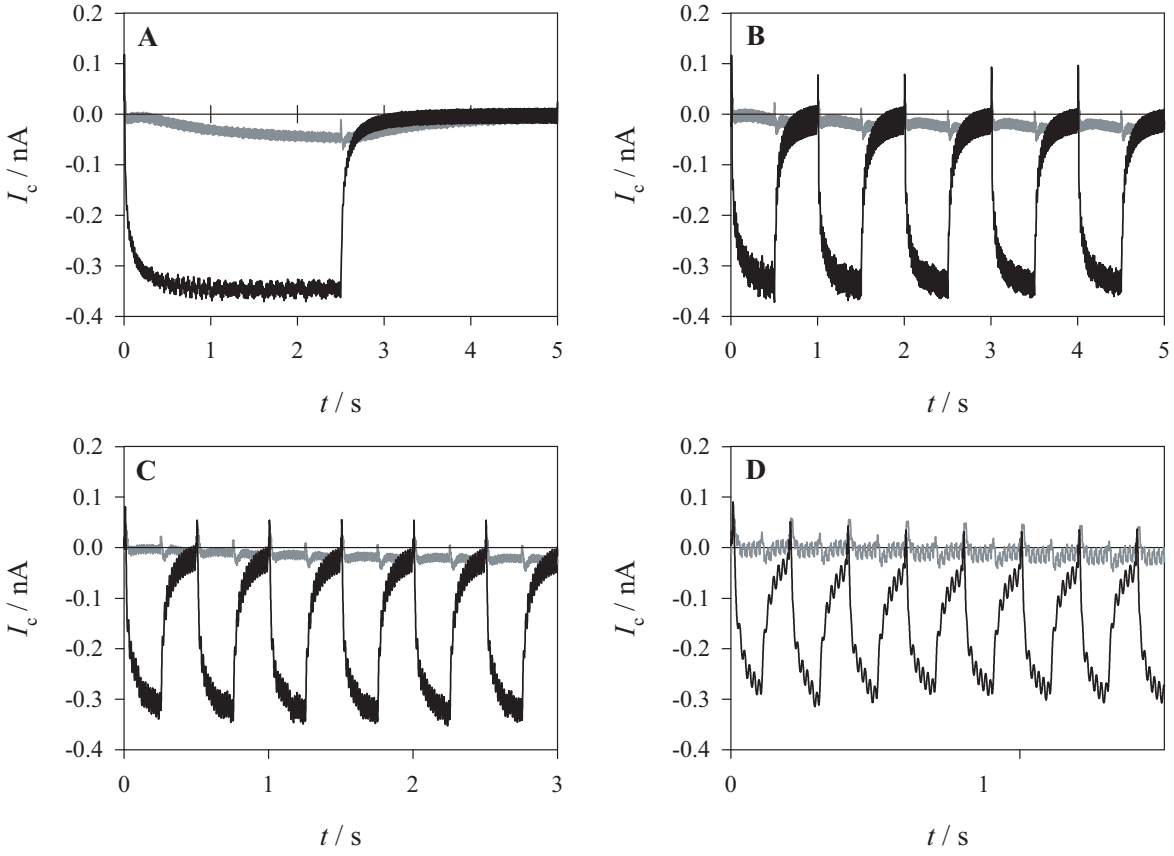

Figure 8. Experimental collector currents measured at different square wave frequencies (applied to the generator electrode) for two different dual disk electrodes, one having g = 1.1 and the other having g = 7.2. Square wave frequencies are (A) 0.2 Hz, (B) 1.0 Hz, (C) 2.0 Hz, and (D) 5 Hz. Conditions: 1.00 mM $Ru(NH_3)_6^{3+}$, $E_{gen} = \pm 0.4$ V, $E_{col} = +0.4$ V.

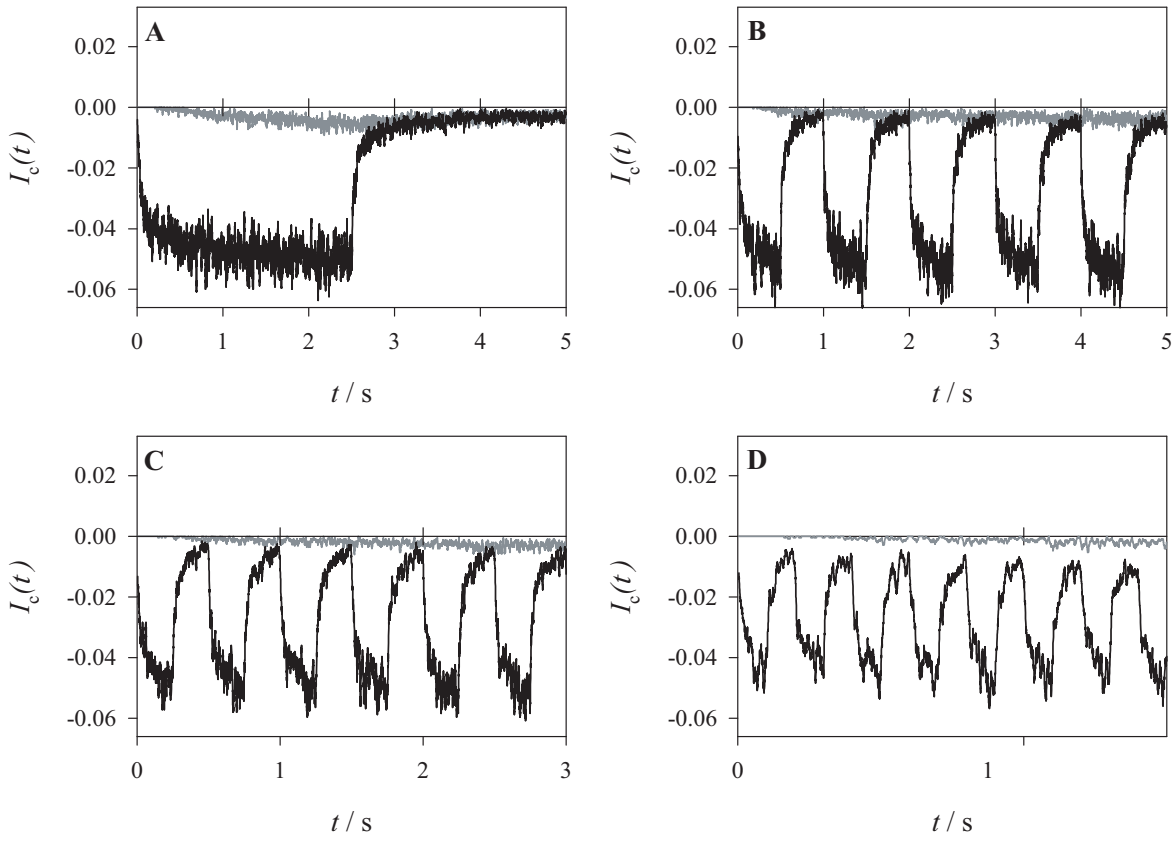

Figure 9. Simulated collector currents for different square wave frequencies for the dual disk electrodes of Figure 8. The black line is the simulation result for $g = 0.9$ and the gray line is the simulation result for $g = 7.2$. Square wave frequencies are (A) 0.2 Hz, (B) 1.0 Hz, (C) 2.0 Hz, and (D) 5 Hz. Conditions: Average of 100 simulations, $\alpha_1 = \alpha_2 = 5$, $\rho = 0.05$, $M = 12$, $X = 130 + \alpha_1 g$, $Y = 120$, and $Z = 60$.